


Interpreting the three-dimensional orientation of vascular canals and cross-sectional geometry of cortical bone in birds and bats

Isaac V. Pratt,¹  James D. Johnston,² Ernie Walker³ and David M. L. Cooper¹

¹Department of Anatomy & Cell Biology, University of Saskatchewan, Saskatoon, SK, Canada

²Department of Mechanical Engineering, University of Saskatchewan, Saskatoon, SK, Canada

³Department of Archaeology & Anthropology, University of Saskatchewan, Saskatoon, SK, Canada

Abstract

Cortical bone porosity and specifically the orientation of vascular canals is an area of growing interest in biomedical research and comparative/paleontological anatomy. The potential to explain microstructural adaptation is of great interest. However, the determinants of the development of canal orientation remain unclear. Previous studies of birds have shown higher proportions of circumferential canals (called laminarity) in flight bones than in hindlimb bones, and interpreted this as a sign that circumferential canals are a feature for resistance to the torsional loading created by flight. We defined the laminarity index as the percentage of circumferential canal length out of the total canal length. In this study we examined the vascular canal network in the humerus and femur of a sample of 31 bird and 24 bat species using synchrotron micro-computed tomography (micro-CT) to look for a connection between canal orientation and functional loading. The use of micro-CT provides a full three-dimensional (3D) map of the vascular canal network and provides measurements of the 3D orientation of each canal in the whole cross-section of the bone cortex. We measured several cross-sectional geometric parameters and strength indices including principal and polar area moments of inertia, principal and polar section moduli, circularity, buckling ratio, and a weighted cortical thickness index. We found that bat cortices are relatively thicker and poorly vascularized, whereas those of birds are thinner and more highly vascularized, and that according to our cross-sectional geometric parameters, bird bones have a greater resistance to torsional stress than the bats; in particular, the humerus in birds is more adapted to resist torsional stresses than the femur. Our results show that birds have a significantly ($P = 0.031$) higher laminarity index than bats, with birds having a mean laminarity index of 0.183 in the humerus and 0.232 in the femur, and bats having a mean laminarity index of 0.118 in the humerus and 0.119 in the femur. Counter to our expectation, the birds had a significantly higher laminarity index in the femur than in the humerus ($P = 0.035$). To evaluate whether this discrepancy was a consequence of methodology we conducted a comparison between our 3D method and an analogue to two-dimensional (2D) histological measurements. This comparison revealed that 2D methods significantly underestimate ($P < 0.001$) the amount of longitudinal canals by an average of 20% and significantly overestimate ($P < 0.001$) the laminarity index by an average of 7.7%, systematically mis-estimating indices of vascular canal orientations. In comparison with our 3D results, our approximated 2D measurement had the same results for comparisons between the birds and bats but found significant differences only in the longitudinal index between the humerus and the femur for both groups. The differences between our 3D and pseudo-2D results indicate that differences between our findings and the literature may be partially based in methodology. Overall, our results do not support the hypothesis that the bones of flight are more laminar, suggesting a complex relation between functional loading and microstructural adaptation.

Key words: Micro-CT; bone vascularity; laminar bone; bone microstructure.

Correspondence

Isaac V. Pratt, Department of Anatomy & Cell Biology, University of Saskatchewan, Health Sciences Building 107 Wiggins Road Saskatoon, SK, Canada S7N 5E5. E: isaac.pratt@usask.ca

Accepted for publication 9 February 2018

Article published online 8 March 2018

Introduction

Bone is a complex tissue, with many functions in the body. In particular, cortical bone and the porosity inside it are important factors in the overall strength of a bone

(Ammann & Rizzoli, 2003; Cooper et al. 2016). In cortical bone microstructure, the pattern seen in the arrangement of the vascular canal network is thought to occur in response to growth as a juvenile, functional adaptation to use during life, and maintenance and metabolic needs throughout life. These signals are of great interest in using bone as a tool for analysing the life history of vertebrates (de Ricqlès et al. 1991; Ricqlès et al. 2000; Cubo et al. 2008; Mitchell & van Heteren, 2015; Marelli & Simons, 2014) and for reconstructing behaviour of extinct vertebrates (Seymour et al. 2012; Padian et al. 2016). As a biological system, the overlap of distinct factors on the same tissue creates confounding effects that interfere with a clear analysis. This presents challenges in deciphering what any given pattern may mean.

The vascular canal network in cortical bone initially develops during the primary formation of bone. During this process, bone is either deposited rapidly as woven bone or more slowly as lamellar bone. In lamellar bone, large vascular spaces are present during the initial development of the bone. As the tissue ossifies it surrounds the spaces, filling them in to become primary osteons (Maggiolo, 2011). In humans and many other larger animal species, bone undergoes a controlled process of renewal called remodelling. This process creates secondary osteons and the canals within them later in life.

Canals can be classified as having four main orientations: longitudinal – where the canals are parallel to the long axis of the bone; radial – where the canals are perpendicular to the tangent at the periosteal boundary; circumferential – where the canals lie parallel to the tangent at the periosteal boundary; and oblique – falling in between the other categories. As canals exist in three dimensions, they often do not fall exactly into one or another category. For example, a canal can be radial in the plane of section but at an angle in the longitudinal plane. Here we followed the classification in Pratt & Cooper (2017) shown below in Table 2. De Margerie et al. (2002) created a new measurement, the index of laminarity, based on the proportion of the circumferential canal area to the total canal area examined. They looked at the orientation of vascular canals in bones of mallard ducks and found a difference between wing bones and hindlimb bones, with the wing bones being significantly more laminar. They noted a dichotomy in the bones they studied at around 50% circumferential canals and called bones at or higher than that level 'laminar'. They proposed that this laminar arrangement was an adaptation to better resist torsional loading, the predominant loading regime in active flight (Pennycuik, 1967; Swartz et al. 1992; de Boef, 2008). Other evidence for canal orientation responding to loading patterns exists in humans (Hert et al. 1994; Petrtyl et al. 1996) where slight deviations to longitudinal orientations of canals are thought to reflect bending as the dominant loading force, and in rats where a 6-month period of paralysis of a limb (removing all loading) dramatically alters

the orientation of vascular canals (Britz et al. 2012). Following these lines, Rothschild & Panza (2007) investigated whether the degree of laminarity was a possible risk factor in bird lower limb bones with osteoarthritis, although they found no link present. If canal orientation is driven by the forces of functional loading we would expect to find similar orientation patterns in both bats and birds, with a higher laminar index in the humerus than in the femur.

The other factor which is potentially responsible for a laminar pattern in cortical bone is the growth rate during development (Lee & Simons, 2015). However, a study by de Margerie et al. (2002) showed that the orientation of primary canals in mallards was independent of growth rate. Other studies (de Margerie et al. 2004; de Boef & Larsson, 2007) suggest that laminar bone grows more slowly and bone with radial canals grows the fastest. De Margerie et al. (2004) have suggested that radial canals have the most detrimental effect on mechanical resistance of shear stress of all the canal orientations. Kuehn et al. (2017) showed that laminarity in the emu hindlimb increased with age, and they proposed that this was due to biomechanical loading as the animal increased in size. Most birds experience very rapid growth, as they need to acquire flight quickly to feed themselves (Erickson et al. 2001); bats, however, experience slower growth (Kunz & Stern, 1995; Lee & Simons, 2015). Skedros & Hunt (2004) found a significantly higher laminarity index in adult turkey ulnae than in sub-adult bones. They suggest that the change in laminarity from sub-adult to adult may be caused by loading history or by ontogenetic changes in growth rate, and that the changes in growth rate may be the stronger factor. Skedros & Hunt (2004) also measured the collagen fibre orientation (CFO) throughout the cortex and found a strong correlation between the laminar index and predominant CFO ($r = 0.735$ in sub-adults, $r = 0.866$ in adults, $P < 0.01$). They suggest that CFO is more closely linked to the strain distributions which can differentiate torsion from bending, and that the vascular orientation is more strongly influenced by the rate of osteogenesis. If this is the case then we would expect to find different patterns of canal orientation between birds and bats, with bats presenting more circumferential canals as they experience slower bone growth.

Cross-sectional geometric parameters describe the shape, distribution, and amount of bone present in a cross-section. Measured parameters and calculated indices are known to reflect the resistance of a bone to mechanical loading, including torsion, bending, axial compression and tension, and local buckling (Turner & Burr, 1993). Analysis of cross-sectional geometry is a common technique in cortical bone assessment (Johnston et al. 2014) and has been used to analyse both human and non-human bone (Lieberman et al. 2004; Pearson & Lieberman, 2004; de Margerie et al. 2005; Marelli & Simons, 2014; Cosman et al. 2016). The principal area moment of inertia (I) reflects the resistance of a bone to bending around a chosen axis. In particular, we

calculated maximum and minimum principal area moments of inertia (I_{max} , I_{min}), which reflect the highest and lowest resistances of the bone. The ratio I_{max}/I_{min} can be used to infer how even the bones experience loads in different directions, with a value of 1 representing equal loads and values farther away from 1 reflecting more asymmetrical loading. The polar area moment of inertia (I_p) is calculated as the sum of I_{max} and I_{min} and reflects the bone resistance to torsional loading (Marelli & Simons, 2014). The principal section modulus is a direct measure of the strength of a bone and its resistance to bending in a specified axis. Similar to the polar area moment of inertia, we calculated the maximum and minimum (Z_{max}/Z_{min}) section moduli and a polar section modulus (Z_p), which reflects torsional strength (Johnston et al. 2014). We also calculated the buckling ratio, a measure of the instability of a bone, reflecting its ability to resist local fractures. Cortical area can be used as a measure of the resistance of a bone to axial compression (Lieberman et al. 2004). We also quantified cortical thickness relative to the cortical area to get a measure of thickness independent of the size of the bone. Higher cortical thickness increases bone resistance to bending but is a less important factor than the outer diameter of a bone (Ammann & Rizzoli, 2003). However, the size of a bone is primarily driven by the size of the animal, so a comparison of a weighted cortical thickness may be more informative for determining what forces a bone is responding to. The shape of a bone is also important in mechanical strength. Elliptical bones are interpreted as having higher resistance to bending along the major axis, whereas more circular bones have more even bending resistance in every direction and are more resistant to torsional loading (de Margerie et al. 2005).

We hypothesized that loading environment is the most important factor in bone vascular canal orientation. We set out to test this by comparing the orientation of vascular canals in the humerus – the main bone in the wing, and the femur – the main bone in the hindlimb in active flying birds and bats. We used synchrotron computed tomography (SR Micro-CT) to produce three-dimensional (3D) maps of the cortical networks in both groups and measure the orientation of the canals within the networks. We followed the method laid out in Pratt & Cooper (2017) with minor adjustments. By comparing the canal networks between wing bones and hindlimb bones we sought to determine whether the presence or absence of a pattern is related to the action of the limb. By comparing between birds and bats, the two extant actively flying vertebrate groups, we looked to see whether there is a common orientation pattern present in the bones of both groups that could be a response to the shared loading pattern created by flight. If loading environment does determine canal orientation, we expected to find similar orientation patterns between the groups, and a higher laminarity index in the humerus than the femur. We also expected the humeri to be more circular

and to have higher polar section moduli than the femora. Based on this we expected to see correlations between the laminarity index and geometric parameters representing torsional resistance, and between the longitudinal index and geometric parameters representing bending resistance.

Materials

The study incorporated nine bat species and 22 bird species with isolated bones from 54 individuals scanned in total (see Table 1). A scan was taken of the right humerus and right femur of each individual. The sampled bat taxa represent both of the major bat clades Yinpterochiroptera and Yangochiroptera. The bird species were chosen to cover the major groups of large birds as best as possible and include 10 orders – Accipitriformes, Anseriformes, Falconiformes, Galliformes, Gaviiformes, Gruiformes, Pelecaniformes, Psittaciformes, Strigiformes, and Suliformes. We chose the largest locally accessible species of bats and birds because bones below a certain size often have fewer canals (de Buffrénil et al. 2008; Lee & Simons, 2015). The bat specimens were borrowed from the Department of Natural History – Mammology at the Royal Ontario Museum (Toronto, Canada). The bird specimens were borrowed from the Zooarchaeology collection in the Department of Archaeology and Anthropology at the University of Saskatchewan (Saskatoon, Canada). The bone specimens were all professionally skeletonized by boiling or dermestids and were wild collected, obtained from local zoo collections or donated by hunters or conservation officers. The specimens were well-preserved and there was no evidence of deterioration visible in the microarchitecture or macroarchitecture. Animal ethics approval was granted by the University of Saskatchewan Animal Research Ethics Board of the University Committee on Animal Care and Supply (protocol 2013-0114) and by the Canadian Light Source.

Methods

Micro-CT

We used phase contrast enhanced synchrotron micro-computed tomography to image our samples (Tafforeau et al. 2006; Arhatari et al. 2011). We scanned the humerus and femur at midshaft of each individual (see Fig. 1). Micro-CT imaging was performed at the BioMedical Imaging and Therapy (BMIT) beamlines (Wysokinski et al. 2007, 2015), part of the Canadian Light Source (CLS) synchrotron facility. We used both the bend magnet (BM) and insertion device (ID) beamlines which comprise the BMIT facility, depending on availability. Imaging quality was comparable between the two beamlines; however, scanning using the ID beamline was much faster due to its higher X-ray flux, and the ID beamline has a taller field of view. Both beamlines were used with the same camera/detector set-up. We used a Hamamatsu C9300-124 optical camera paired with the Hamamatsu A40 X-ray converter to take projection images with an effective pixel size of $4.3 \mu\text{m}$ at 32 keV. This camera gives a field of view (FOV) of 11 mm in width. Many of the bones in the sample have a shaft diameter greater than 11 mm, requiring a larger FOV. We used two methods to overcome this limitation. By moving the centre of rotation of the scan and rotating through 360° the FOV can be increased up to 18–19 mm. Alternatively, the camera can be offset so that two projection images are taken and stitched together for each rotation step. Because of the wide FOV provided by the open gantry micro-CT

Table 1 List of specimens used. If not otherwise noted, $n = 1$.

Birds	Bats
Mallard (<i>Anas platyrhynchos</i>)	Egyptian Fruit Bat (<i>Rousettus aegyptiacus</i>) ($n = 4$)
White-fronted goose (<i>Anser albifrons</i>)	Great Fruit-eating Bat (<i>Artibeus literatus</i>) ($n = 4$)
Snow goose (<i>Anser caerulescens</i>)	Grey-headed flying fox (<i>Pteroptus poliocephalus</i>)
Golden eagle (<i>Aquila chrysaetos</i>)	Hairless bat (<i>Cheiromlis torquatus</i>) ($n = 4$)
Yellow-blue macaw (<i>Ara ararauna</i>)	Indian flying fox (<i>Pteroptus giganteus</i>) ($n = 4$)
Great blue heron (<i>Ardea herodias</i>) ($n = 2$)	Large flying fox (<i>Pteroptus vampyrus</i>)
Short-eared owl (<i>Asio flammeus</i>)	Lyle's flying fox (<i>Pteroptus lylei</i>) ($n = 3$)
Ruffed grouse (<i>Bonasa umbellus</i>)	Spectral bat (<i>Vampyrus spectrum</i>) ($n = 4$)
American bittern (<i>Botaurus lentiginosus</i>)	Straw-coloured fruit bat (<i>Eidolon helvum</i>)
Great horned owl (<i>Bubo virginiana</i>) ($n = 3$)	
Red-tailed hawk (<i>Buteo jamaicensis</i>) ($n = 2$)	
Rough-legged hawk (<i>Buteo lagopus</i>)	
Swainson's hawk (<i>Buteo swainsoni</i>)	
Turkey vulture (<i>Cathartes aura</i>)	
Greater sage-grouse (<i>Centrocercus urophasianus</i>)	
Common loon (<i>Gavia immer</i>)	
Whooping crane (<i>Grus americana</i>)	
Sandhill crane (<i>Grus canadensis</i>)	
Bald eagle (<i>Haliaeetus leucocephalus</i>)	
Snowy owl (<i>Nyctea scandiaca</i>) ($n = 2$)	
American white pelican (<i>Pelecanus erythrorhynchos</i>) ($n = 2$)	
Double-crested cormorant (<i>Phalacrocorax auritus</i>)	
Total $n = 30$	Total $n = 24$

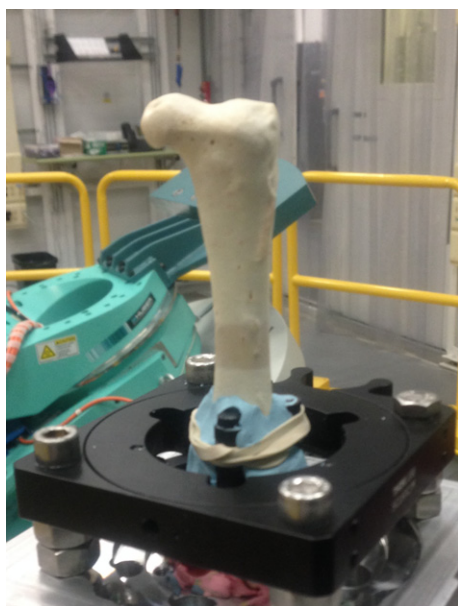


Fig. 1 This image shows an example of sample mounting at the beamline. Pictured here is an American white pelican femur. Each specimen was mounted using a self-centring mount and secured with modelling clay so that the shaft of the bone was stable in the field of view of the detector. On this sample, discoloration on the surface of the cortex is visible from the area scanned.

system at BMIT, we were able to scan our specimens completely non-destructively. The height of the FOV was 2 mm on the BM and 4 mm on the ID beamline. Each specimen was scanned with

exposure times ranging from 0.5 to 1.5 s per projection. The exact exposure time depended on the synchrotron beam ring current, which decays from a peak of 250 mA over time. Flat and dark frames were collected before each scan to correct for noise in the detector and the X-ray beam. An aluminium filter with an effective thickness of 1.1 mm was used to eliminate any stray low energy harmonics. Our scans were optimized for in line phase contrast using a propagation distance of 50 cm.

Image processing

The main steps in the image processing are illustrated in Fig. 2. A custom software package was developed using the IMAGEJ (ImageJ, NIH) scripting platform to perform most of the data processing. The micro-CT projections were initially processed to correct for detector and beam noise using flat and dark projections, and reconstructed using NRECON (Bruker SkyScan, Kontich BE), a commercial software package. NRECON provides graphics card acceleration, allowing for rapid reconstruction of large data sets. We used AMIRA (FEI Company, USA) to perform the main data processing – thresholding, segmenting, and skeletonizing the reconstructed micro-CT slices to extract the canal network from the bone as a lineset. Our analysis closely follows the method described in Pratt & Cooper (2017).

Each canal lineset was initially processed to identify branch points in the canal network and subsample the network into a series of line segments of a defined length. This allows for better measurement of the variability of orientation in the network, especially of curved canals. We used a distance of 23 pixels (100 μm), roughly the equivalent of a standard histological slice. We measured the position of the bone centroid in each slice and the three-dimensional orientation of each line segment in the subsampled network

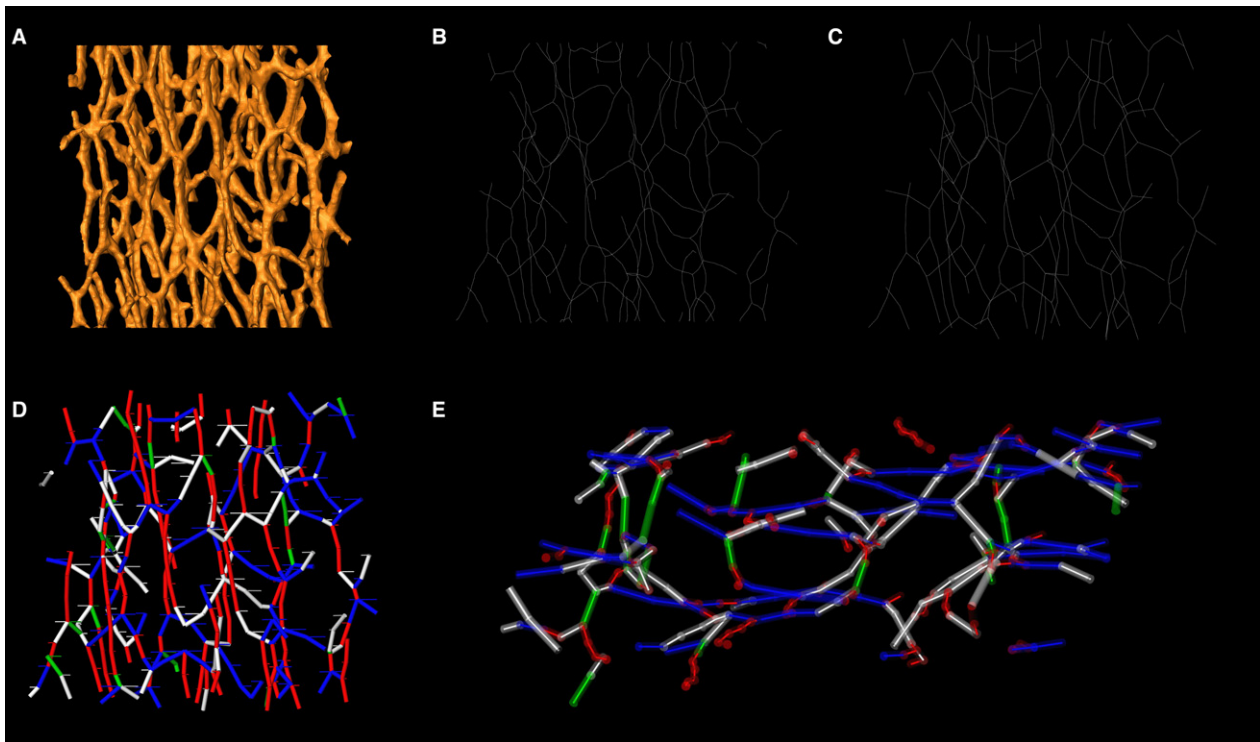


Fig. 2 Processing steps for data analysis using a small region of interest (ROI) selected from the humerus scan of a Swainson's hawk. (A–D) Longitudinal sections parallel to the endosteal surface. The initial canal render is shown in (A), followed by the skeleton in (B), and the subsampled network in (C), clearly illustrating the close preservation of the original orientation of the canal segments. (D,E) Measured 3D orientation categories of the canal segments (thick lines) and their projected 2D analogues (thin lines). Red, longitudinal canals; green, radial canals; blue, circumferential canals; white, oblique canals. (E) Transverse section, looking top down, showing that the 2D analogues have the same orientation in the transverse section as the original 3D canal segments.

Table 2 Canal categories.

Canal category	Phi	Theta
Longitudinal	67.5–90	0–90
Circumferential	0–67.5	67.5–90
Radial	0–67.5	0–22.5
Oblique	[0–22.5, 67.5–90], [22.5–67.5]	[22.5–67.5], [0–90]

relative to the position of the centroid. Two angles are measured, theta and phi. Phi is the angle between a canal segment and the long axis of the bone and is used to determine whether a canal is longitudinal. Theta is the angle between a canal and a line from the bone centroid to midpoint of that canal. Theta is used to differentiate between radial and circumferential canals. By using both angles we were able to differentiate fully between all four bone categories, including oblique canals. This allows us to classify whether each line segment is longitudinal, radial or circumferential (see figure 5). We classified canal segments following the criteria in de Margerie (2002) and Pratt & Cooper (2017), as shown in Table 2. In contrast to the method shown earlier in Pratt & Cooper (2017), we weighted the orientation measure by the 3D length of each line segment, so that shorter line segments (those segments under 100 μm) that are less than the separation distance have less effect

on the overall measures of the scan. We then calculated the laminar, radial, and longitudinal indices as the ratio of the sum of the length of all the circumferential, radial or longitudinal canal segments over the total length of all canal segments (see Eq. 1). We use canal length instead of the canal area measure used by de Margerie et al. (2002) because the length reflects the proportions of canals in the network more accurately than area does, which underestimates longitudinal canals. Canal length is a 3D measure which we can measure with micro-CT but which cannot be measured in histology.

$$\text{Laminar index} = \frac{\sum \text{Canal Segment Length}_{\text{circumferential}}}{\sum \text{Canal Segment Length}_{\text{all}}}$$

Eq. 1. Laminar index calculation. Calculations for radial and longitudinal indices are analogous.

To see how the 3D measure performs against traditional 2D methods such as histology we performed a kind of pseudo 2D measurement on the same micro-CT scans. In the orientation measurement, instead of using the full canal segment length, we used the projected 2D length in the cross-sectional plane.

Cross-sectional geometry

The middle slice of each scan was selected for analysis using cross-sectional geometry metrics. The slices were masked and the porosity

filled in. Custom algorithms (MATLAB XX, MathWorks, Natick, MA, USA) were used to measure the geometric parameters and strength indices. The metrics measured included the ratio of principal maximum and minimum area moments of inertia (I_{max}/I_{min}), polar area moment of inertia (I_p), the ratio of principal maximum and minimum section moduli (Z_{max}/Z_{min}), polar section modulus (Z_p), buckling ratio (BR), cortical thickness (t_c), cortical area (a_{cort}), and circularity. To account for differences in size we created a cortical thickness index defined as the ratio of cortical thickness over cortical area.

Principal area moments of inertia were calculated based on traditional methods, with the polar area moment of inertia calculated as the sum of the minimum and maximum area moments of inertia. Principal section moduli were calculated by dividing the equivalent principal area moment of inertia by the corresponding maximum distances to the outer periosteal edges from the principal neutral axes. The polar section modulus was defined following Johnston et al. (2014) by dividing the polar area moment of inertia by the maximum outer radius of the bone. The buckling ratio was calculated as the ratio of total area to cortical area (Sievänen et al. 2016). Cortical thickness was measured using the unrolling approach (Johnston et al. 2014). Circularity was defined as the ratio of the total bone area to the area of the smallest inscribing circle (Zebaze et al. 2005).

Statistical analysis was performed with SPSS version 24 (IBM, USA). We used repeated measures two-way MANOVAS to compare the three orientation indices, the geometric parameters, and the strength indices between the two taxonomic groups and the two bones for both the 3D and the pseudo-2D data. A one-way repeated measures ANOVA was used to compare the pseudo-2D and 3D results. Linear regression analysis was used to look for correlations between geometric and strength parameters and orientation indices.

Results

Descriptive statistics are shown in Table 3 for the 3D measurements. The comparison between birds and bats is shown in Table 4 and the comparison between humerus and femur in Table 5 for both the 3D and pseudo-2D methods. We consider a *P*-value of less than 0.05 statistically significant; all *P*-values are shown in the tables. The comparison between the two measurement methods is shown in Table 6. For the main 3D analysis, we found that birds have a higher laminar index compared with bats in the humerus and femur. The birds also had a lower radial index in the humerus and a lower longitudinal index in the femur. The results for the pseudo-2D analysis mirrored these findings.

We also found that in birds the humerus had a lower laminarity index than the femur and a higher longitudinal index. In contrast, the pseudo-2D method only found significant differences in the longitudinal index, higher in the humerus than the femur in the birds and lower in the bats. We found differences between the two methods for all three measures, with the laminar and radial indices higher in the pseudo-2D measure and the longitudinal index lower. In both the birds and the bats, the overall highest category of canals was longitudinal, followed by radial, and the lowest was laminar.

We found several differences in the cortical bone geometrical parameters. Both the Z_p and I_p were higher in birds

Table 3 Descriptive statistics for the 3D measurement style.

Variable	Tax group	Bone	Mean	SD
3D laminar index	Birds	Humerus	0.183	0.057
		Femur	0.232	0.075
	Bats	Humerus	0.118	0.115
		Femur	0.119	0.118
3D Radial Index	Birds	Humerus	0.218	0.064
		Femur	0.243	0.080
	Bats	Humerus	0.309	0.185
		Femur	0.273	0.196
3D Longitudinal Index	Birds	Humerus	0.471	0.093
		Femur	0.383	0.094
	Bats	Humerus	0.507	0.201
		Femur	0.537	0.239
Z_p	Birds	Humerus	94.321	80.976
		Femur	10.211	49.33
	Bats	Humerus	57.499	10.126
		Femur	3.499	3.955
I_p	Birds	Humerus	589.053	696.29
		Femur	27.734	348.78
	Bats	Humerus	307.387	36.561
		Femur	6.951	10.558
Buckling ratio	Birds	Humerus	6.545	1.646
		Femur	3.722	1.1822
	Bats	Humerus	6.993	0.4745
		Femur	3.464	0.4723
I_{max}/I_{min}	Birds	Humerus	1.434	0.1627
		Femur	1.277	0.1646
	Bats	Humerus	1.218	0.1858
		Femur	1.314	0.1805
Z_{max}/Z_{min}	Birds	Humerus	1.241	0.093
		Femur	1.145	0.0866
	Bats	Humerus	1.097	0.0974
		Femur	1.149	0.0757
Cortical thickness index	Birds	Humerus	0.039	0.014
		Femur	0.104	0.0181
	Bats	Humerus	0.046	0.0296
		Femur	0.163	0.0568
Circularity	Birds	Humerus	0.811	0.0491
		Femur	0.828	0.0623
	Bats	Humerus	0.828	0.0557
		Femur	0.812	0.0782

than bats in both the humerus and the femur, and higher in the humerus than the femur in birds. The buckling ratio was higher in birds than in bats in both the humerus and the femur. We found that both I_{max}/I_{min} and Z_{max}/Z_{min} were higher in birds than in bats in the humerus. I_{max}/I_{min} and Z_{max}/Z_{min} were also both higher in the humerus than in the femur in birds. Using the cortical thickness index we found that both the humerus and the femur of bats were thicker compared with birds, and that the femur was thicker than the humerus in bats. We found no correlations between the geometric parameters representing torsional resistance and the laminarity index, and no correlations between the

Table 4 Comparison between birds and bats. A positive mean difference means the birds are have a higher value than the bats.

Variable	Bone	Mean difference	SE	Significance
3D laminar index	Humerus	0.059	0.027	0.031
	Femur	0.121	0.028	0.000
3D radial index	Humerus	-0.113	0.034	0.002
	Femur	-0.049	0.043	0.267
3D longitudinal index	Humerus	-0.010	0.039	0.791
	Femur	-0.147	0.052	0.007
Pseudo-2D laminar index	Humerus	0.090	0.037	0.018
	Femur	0.148	0.038	0.000
Pseudo-2D radial index	Humerus	-0.166	0.038	0.000
	Femur	-0.079	0.045	0.091
Pseudo-2D longitudinal index	Humerus	-0.024	0.030	0.421
	Femur	-0.165	0.046	0.001
Z_p	Humerus	80.577	18.391	0.000
	Femur	50.861	10.871	0.000
I_p	Humerus	544.293	158.423	0.001
	Femur	280.055	75.549	0.001
Buckling ratio	Humerus	2.912	0.368	0.000
	Femur	3.477	0.252	0.000
I_{max}/I_{min}	Humerus	0.195	0.042	0.000
	Femur	-0.085	0.051	0.105
Z_{max}/Z_{min}	Humerus	0.126	0.023	0.000
	Femur	-0.048	0.025	0.059
Cortical thickness index	Humerus	-0.060	0.007	0.000
	Femur	-0.109	0.012	0.000
Circularity	Humerus	-0.018	0.014	0.190
	Femur	0.012	0.019	0.525

Variables in bold are statistically significant.

geometric parameters representing bending resistance and the longitudinal index.

Discussion

The traditional method for studying cortical bone porosity has been undecalcified bone histology. Micro-CT is a relatively new technique (Feldkamp et al. 1989) that has increasingly been applied to cortical bone microstructure. In comparison with histology, micro-CT is 'less destructive' – depending on the system and sample it can be completely non-destructive, as in our case. Non-destructive imaging methods preserve the specimens for future analysis and make obtaining access to rare materials much easier. Micro-CT is typically lower resolution than histology – only the highest resolution scans are able to capture osteon boundaries (Arhatari et al. 2011; Cooper et al. 2011; Maggiano et al. 2015; Andronowski et al. 2017). This means most micro-CT scans are not able to differentiate primary from secondary canals. Scan quality varies drastically between micro-CT systems and the best systems are available only at synchrotron research facilities, where research time is limited; However, the fundamental advantage of micro-CT is

Table 5 Comparison between humerus and femur. A positive mean difference means the humerus has a higher value than the femur.

Variable	Tax group	Mean difference	SE	Significance
3D laminar index	Birds	-0.040	0.018	0.035
	Bats	0.022	0.022	0.304
3D radial index	Birds	-0.032	0.027	0.255
	Bats	0.033	0.032	0.315
3D longitudinal index	Birds	0.085	0.033	0.013
	Bats	-0.051	0.039	0.196
Pseudo-2D laminar index	Birds	-0.034	0.027	0.211
	Bats	0.024	0.032	0.445
Pseudo-2D radial index	Birds	-0.026	0.031	0.400
	Bats	0.062	0.036	0.095
Pseudo-2D longitudinal index	Birds	0.062	0.029	0.037
	Bats	-0.079	0.034	0.024
Z_p	Birds	37.217	5.821	0.000
	Bats	7.501	6.888	0.282
I_p	Birds	288.068	60.160	0.000
	Bats	23.829	71.182	0.739
Buckling ratio	Birds	-0.341	0.228	0.141
	Bats	0.224	0.269	0.409
I_{max}/I_{min}	Birds	0.213	0.042	0.000
	Bats	-0.068	0.050	0.180
Z_{max}/Z_{min}	Birds	0.146	0.023	0.000
	Bats	-0.028	0.027	0.301
Cortical thickness index	Birds	-0.007	0.004	0.078
	Bats	-0.055	0.004	0.000
Circularity	Birds	-0.012	0.014	0.387
	Bats	0.018	0.017	0.274

Variables in bold are statistically significant.

Table 6 Comparison between pseudo-2D method and 3D method.

Measure	Mean difference	SE	Significance
Laminar index	0.077	0.004	0.000
Radial index	0.094	0.005	0.000
Longitudinal Index	-0.209	0.005	0.000

its ability to capture the full 3D vascular canal network in a complete bone and to capture many more canals than are present in a single histological slice. This study is the first to use micro-CT to test hypotheses about canal orientation in 3D. Previous studies on canal orientation using micro-CT have only been able to differentiate between longitudinal canals and transverse canals (Britz et al. 2012; Jast & Jasiuk, 2013) and have not been able to differentiate between radial and circumferential canals until Pratt & Cooper (2017). Our study relied on the synchrotron system to provide a wider field of view than most laboratory-based micro-CT systems, allowing the imaging of the full bone cross-section non-destructively. Previous studies have used histology and attempted to infer a 3D orientation (de Boef & Larsson, 2007) but this approach is flawed by the assumptions required to generate the measurement. They fit an

ellipse into each canal space and if the minor axis is equal to or greater than 95% of the major axis, assume the canal is longitudinal. This relies on the assumption that canals are very circular in cross-section, an assumption that is not always correct (Hennig et al. 2015). A more fundamental problem in the histological method of analysis is the underestimation of longitudinal canals. The method used by most studies (Rensberger & Watabe, 2000; de Margerie, 2002, 2005; Skedros & Hunt, 2004; Cubo et al. 2005; de Boef et al. 2007; Marelli & Simons, 2014; Lee & Simons, 2015) creates a laminarity index based on the proportion of circumferential canal area out of total canal area. In a histological slice, the area of longitudinal canals measured is underestimated, as only a small cross-section of the canal is measured, as opposed to a transverse section of circumferential or radial canals. This affects the accuracy of any calculations relying on a 'total canal area' metric.

We found that the bat species typically have thick cortices with inconsistent vascularization containing few canals typically concentrated into clusters. The birds have thin cortices tightly packed with canals (see Fig. 3). The bats had a significantly higher cortical thickness index than the birds in both the humerus and the femur. The bats had thicker cortices in the femur than in the humerus, whereas there were no differences in cortical thickness between the bones in the birds. Our results indicated that both the birds and the bats were both very circular (close to 1), with no differences between the groups or the bones. This indicates that both bones are adapted to torsional loading. We found a significantly higher buckling ratio in the birds than in the bats, and no differences between the humerus and the femur. This indicates a higher resistance to local fractures in the bones of the birds. This may be due to the thinner cortices in these animals. We found a significantly higher I_p and Z_p in the birds than in the bats, and a significantly higher I_p and Z_p in the bird humeri than in bird femora. These results suggest that the birds have a greater torsional resistance than the bats and that the humeri in birds have greater torsional resistance than the femora. I_{max}/I_{min} and Z_{max}/Z_{min} were significantly higher in bird humeri than in bat humeri,

and were also higher in the humerus than the femur in birds. These differences indicate that the birds and the bats experience different loads across the major and minor axes. Overall, these data reinforce the idea that the humerus is more adapted to torsional stresses, and suggest that bird bones have a greater resistance to torsional stress than bat bones.

In four bat bones (three femora and one humerus), the cortices were found to be completely absent of vascular canals in the area of the scan (see Fig. 4). Previous studies have noted that bats tend to be poorly vascularized or avascular (Foote & Hrdlicka, 1916; Enlow & Brown, 1958; de Ricqlès et al. 1991; Bennett & Forwood, 2010; Lee & Simons, 2015). Monitor lizards are also known to have inconsistent vascularization, with cortices that can be completely free of vascular canals. De Buffrénil et al. (2008) examined the canal orientation and cortical porosity density in these animals. They found that the presence of canals requires a certain body size, and that canal orientation was a variable feature independent of growth rate. Lee & Simons (2015) propose that the absence of fully vascularized tissue indicates that bats do not have laminar bone and that bone shape is more important in determining torsional resistance. They gave a laminar index of 0 or N/A for all the bats in their sample. We had one specimen in our sample (*Pteropus vampyrus*) of a species present in their sample, and we measured a laminar index of 0.049 in its humerus. Part of the reason for this may be due to the problems with the histology measurement method used. As the bats have few canals, any single plane of section may not accurately reflect the full pattern present in the whole bone. Our results show that although the bats have fewer canals overall and a significantly lower laminar index than the birds, they still contain circumferential canals. The clear differences found between the more laminar birds and the bats are in line with the results found by Lee & Simons (2015). The bats do not have enough circumferential canals to call the bone 'laminar'.

Although de Margerie et al. (2002) set a value of 0.5 for the laminar index as a determinant of laminar bone, none

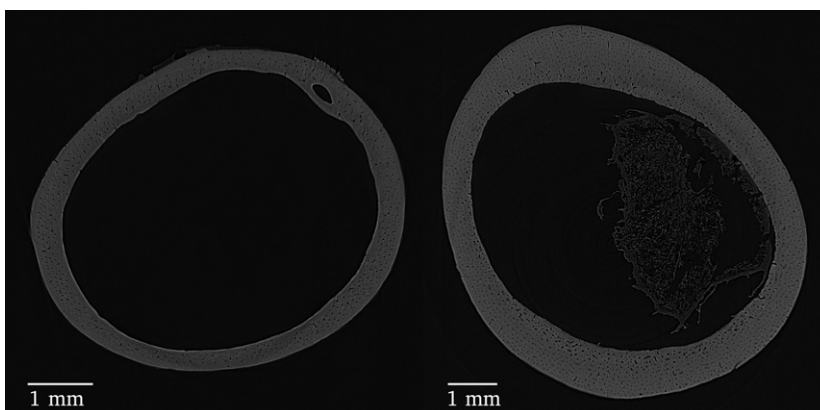
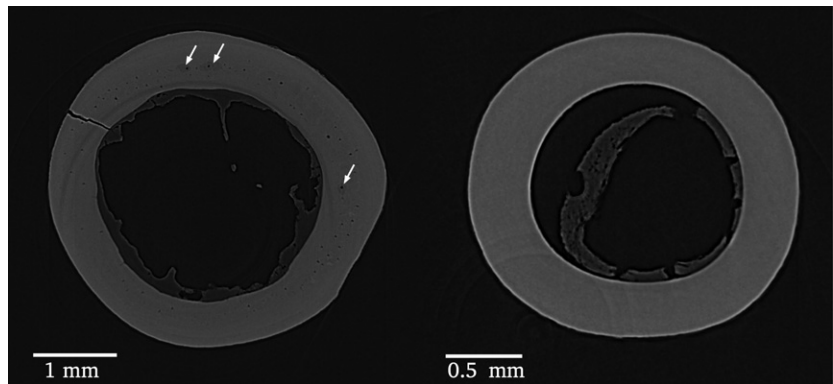


Fig. 3 Bird micro-CT scans. Both images show relatively thin cortices with full vascularization. Right, Swainson's hawk humerus; left, Snowy owl humerus.

Fig. 4 Bat micro-CT scans. Note the relatively thick cortices with typical low vascularization. Complete absence of vascularization can be seen in the right cortex. Some evidence of secondary remodelling can be seen in the cortex on the left (white arrows). Right, Grey-headed flying fox femur; left, Spectral bat femur.



of the bones we scanned had a value that high. Our laminarity index values are much lower than those found by de Margerie et al. (2005) who measured laminarity indices of 0.625 for the humerus and 0.563 for the femur in a sample of 22 birds. Lee & Simons (2015) measured laminarity indices averaging 0.331 overall for humeri of 15 birds, much closer to the values reported here. We found that the bird humeri had an average laminarity index of 0.183, the bird femora an average of 0.232, the bat humeri an average of 0.118, and the bat femora an average of 0.119. In our previous article (Pratt & Cooper, 2017) we measured a laminar index of 0.119 in a rat tibia, well below the mean laminar index for the birds in both humeri and femora. In our comparison, the laminar and radial indices were 0.077 and 0.093 higher in the pseudo-2D measures ($P < 0.001$), whereas the longitudinal index was significantly lower by 0.210 ($P < 0.001$). This indicates that traditional methods underestimate the amount of longitudinal canals by 21% and that previously reported values for laminarity indices may not be reliable.

Several studies have shown that the growth rate of bone differs between the long bones (de Ricqlès et al. 1991; Castanet et al. 2000; Starck & Chinsamy, 2002; de Margerie et al. 2004) with higher growth rates in the hindlimb, and between species, with bats growing slower than birds. De Margerie et al. (2004) suggest that laminar bone is the slowest growing. Skedros & Hunt (2004) found a significantly higher laminar index in adult turkey ulnae than in subadults. They attributed part of this difference to changes in growth rate throughout the lifespan of the animal. We found a significantly higher laminar index in the femur than in the humerus, which could indicate a prioritization of laminar bone over growth rate in the femur, or a prioritization of growth rate over laminar bone in the humerus. Our findings contradict what we expected based on the literature. Previous studies (de Margerie et al. 2002, 2005; de Margerie & Rakotomanana, 2007; Lee & Simons, 2015) have all shown a higher laminar index in the humerus than in the femur. Our 3D results show the opposite of this, a higher laminar index in the femur than in the humerus, but the pseudo-2D measurement shows no difference in the laminar index between the two bones. The pseudo-2D measure found differences in the longitudinal index between the bones in

both groups, whereas the 3D comparison also found a significant difference in the longitudinal index between the humerus and femur in the birds. This indicates that at least part of the disparity between our results and those in the literature originates in the analysis method, with not enough canals measured in the bones and underestimation of longitudinal canals. Another potential explanation for the differences could be high variance in canal orientation between individuals of the same species and between species. The orientation measurements in the bats have relatively high standard deviations (of the same order of magnitude as the means for each group). Our sample contains many different species but few (one to four) individuals per species. The sample contains both female and male individuals, and there is no research on sex differences in cortical canal orientation. Overall, our orientation results run counter to expectations and, taken together with the cortical geometry data which show higher torsional strength in the humerus than in the femur, our results do not support the hypothesis that laminar bone is a response to torsional loading in the wing bones.

In our study we were unable to determine when the patterns seen in the microstructure develop. The micro-CT scans we used are unable to differentiate between primary and secondary canals, so we were unable to say whether the patterns developed early in life during development or later in life through remodelling. Several of the bat scans show large voids in the cortex which are likely remodelling events, and some of the scans show mineralization differences indicating osteon boundaries which are typical of secondary canals (see Fig. 4 for an example in bats). Birds are known to undergo remodelling in maturity and we found some evidence of osteon boundaries in our scans as well. If higher laminarity appears only after flight behaviour manifests, that would be evidence supporting the hypothesis that laminar bone is a response to functional loading. If laminar canals appear during early development, it would require more insight to determine whether this is a response to growth or to an evolutionary pressure for increased resistance to torsional loading. The best avenue for determining this is by way of longitudinal studies on canal orientation, which to the best of our knowledge have never been

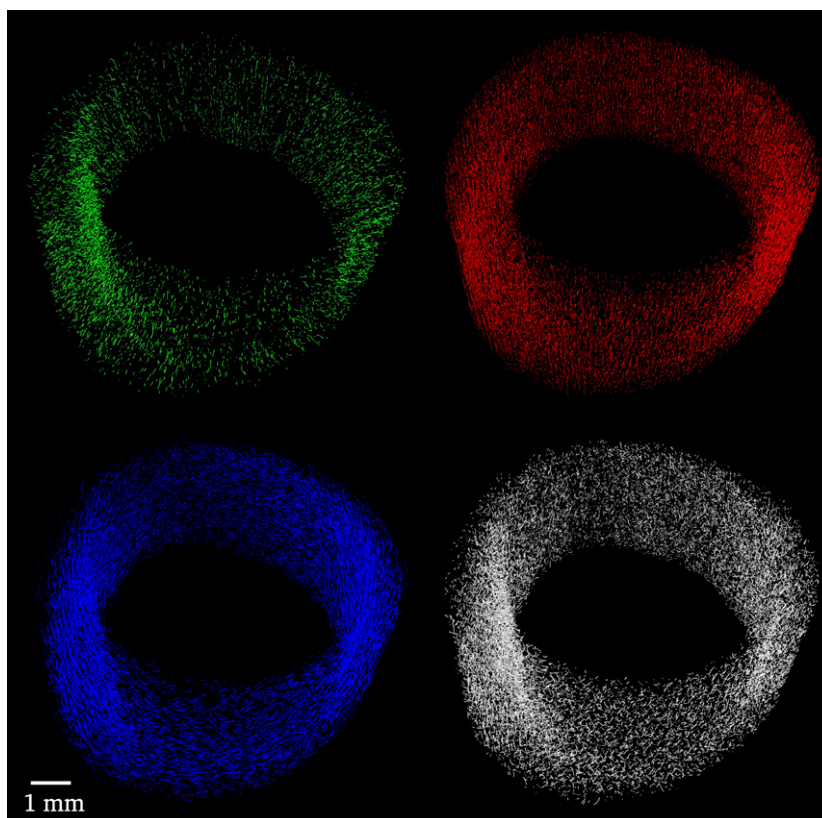


Fig. 5 3D renders of canal segments in a Swainson's hawk humerus with circumferential shown in blue, longitudinal in red, radial in green, and oblique in white.

performed. Previous research in our lab has shown that *in vivo* micro-CT can be applied to image cortical canals in live rats (Pratt et al. 2015). It would be of great interest to apply this technique to a bird model, to determine how the microstructure develops in 3D during ontogeny, especially across the point of acquisition of flight.

Conclusion

Highly vascularized bird cortices and poorly vascularized bat cortices showed clearly different patterns of vascular canal orientation. Although both groups face similar mechanical loads on their wing bones, they seem to have found different strategies to adapt to them. Overall, it remains difficult to assess fully whether a higher laminar index is a response to loading or growth rate; however, this study does not find support for the functional loading hypothesis. Studies seeking to interpret the behaviour of extinct species should be wary of the incomplete state of knowledge in this area and the limitations of histological analysis.

We recommend that any studies of vascular canal orientation use micro-CT rather than histology, to avoid the issue of underestimation of longitudinal canals and to measure instead of infer the theta angle. This study and our previous technical article (Pratt & Cooper, 2017) provide a strong basis for how to proceed with micro-CT analysis of vascular canal orientation.

Future studies should investigate the development of canal orientation throughout the lifespan of the target species, with particular interest in the time period of the acquisition of adult locomotor behaviour. *In vivo* micro-CT imaging provides an excellent opportunity for the acquisition of such data.

Acknowledgements

Support for this research was provided by the Natural Sciences and Engineering Research Council (NSERC) of Canada via a Discovery Grant (RGPIN-2014-05563) to D.M.L.C. D.M.L.C. is further supported by the Canadian Foundation for Innovation and Canada Research Chairs Program. I.V.P. is supported by an NSERC PGS and is a CIHR-THRUST Fellow. Research described in this paper was performed at the Canadian Light Source, which is funded by the Canada Foundation for Innovation, the Natural Sciences and Engineering Research Council of Canada, the National Research Council Canada, the Canadian Institutes of Health Research, the Government of Saskatchewan, Western Economic Diversification Canada, and the University of Saskatchewan. The authors would like to thank Kim Harrison, Dani Kabatoff, and Janna Andronowski for assistance with beamtime.

References

- Ammann P, Rizzoli R (2003) Bone strength and its determinants. *Osteoporos Int* **14**, S13–S18.

- Andronowski JM, Pratt IV, Cooper DML (2017) Occurrence of osteon banding in adult human cortical bone. *Am J Phys Anthropol* **28**, 211.
- Arhatari BD, Cooper DM, Thomas CD, et al. (2011) Imaging the 3D structure of secondary osteons in human cortical bone using phase-retrieval tomography. *Phys Med Biol* **56**, 5265–5274.
- Bennett M, Forwood M (2010) Histomorphometric changes in the wing bones of the fruit bat, *Pteropus poliocephalus*, (Megachiroptera: Pteropidae) in relation to increased bone strain and the failure of a good (?) hypothesis. *Aust Zool* **35**, 341–348.
- Britz HM, Jokihaara J, Leppänen OV, et al. (2012) The effects of immobilization on vascular canal orientation in rat cortical bone. *J Anat* **220**, 67–76.
- Buffrénil V de, Houssaye A, Böhme W (2008) Bone vascular supply in monitor lizards (Squamata: Varanidae): influence of size, growth, and phylogeny. *J Morphol* **269**, 533–543.
- Castanet J, Rogers KC, Cubo J, et al. (2000) Periosteal bone growth rates in extant ratites (ostriche and emu). Implications for assessing growth in dinosaurs. *C R Acad Sci III* **323**, 543–550.
- Cooper DM, Erickson B, Peele AG, et al. (2011) Visualization of 3D osteon morphology by synchrotron radiation micro-CT. *J Anat* **219**, 481–489.
- Cooper DM, Kawalilak CE, Harrison K, et al. (2016) Cortical bone porosity: what is it, why is it important, and how can we detect it? *Curr Osteoporos Rep* **14**, 187–198.
- Cosman MN, Sparrow LM, Rolian C (2016) Changes in shape and cross-sectional geometry in the tibia of mice selectively bred for increases in relative bone length. *J Anat* **228**, 940–951.
- Cubo J, Ponton F, Laurin M, et al. (2005) Phylogenetic signal in bone microstructure of sauropsids. *Syst Biol* **54**, 562–574.
- Cubo J, Legendre P, de Ricqlès A, et al. (2008) Phylogenetic, functional, and structural components of variation in bone growth rate of amniotes. *Evol Dev* **10**, 217–227.
- de Boef M (2008) Signatures of Flight and Running in bone microstructure: an experimental study in helmeted Guinea-fowl (*Numida meleagris*) and applications in the study of the dinosaur-bird transition. *J Vertebr Paleontol* **28**, 70A.
- de Boef M, Larsson HCE (2007) Bone microstructure: quantifying bone vascular orientation. *Can J Zool* **85**, 63–70.
- de Boef M, Larsson H, Horner J (2007) Measurements of vasculature in *Tyrannosaurus rex* show a relationship between growth rate and vasculature orientation. *J Vertebr Paleontol* **27**, 67A.
- de Margerie E (2002) Lamellar bone as an adaptation to torsional loads in flapping flight. *J Anat* **201**, 521–526.
- de Margerie E, Rakotomanana L (2007) *In silico* adaptation of bone vascular microstructure to biomechanical loading mode. *J Morphol* **268**, 1065.
- Enlow DH, Brown SO (1958) A comparative histological study of fossil and recent bone tissues. Part III. *Tex J Sci* **10**, 187–230.
- Erickson GM, Rogers KC, Yerby SA (2001) Dinosaurian growth patterns and rapid avian growth rates. *Nature* **412**, 429–433.
- Feldkamp LA, Goldstein SA, Parfitt AM, et al. (1989) The direct examination of 3-dimensional bone architecture in vitro by computed-tomography. *J Bone Miner Res* **4**, 3–11.
- Footo JS, Hrdlicka A (1916) *A Contribution to the Comparative Histology of the Femur*. Washington, DC: Smithsonian Institution.
- Hennig C, Thomas CD, Clement JG, et al. (2015) Does 3D orientation account for variation in osteon morphology assessed by 2D histology? *J Anat* **227**, 497–505.
- Hert J, Fiala P, Petrtyl M (1994) Osteon orientation of the diaphysis of the long bones in man. *Bone* **15**, 269–277.
- Jast J, Jasiuk I (2013) Age-related changes in the 3D hierarchical structure of rat tibia cortical bone characterized by high resolution micro-CT. *J Appl Physiol (1985)* **114**, 923–933.
- Johnston JD, Liao L, Dolovich AT, et al. (2014) Magnetic resonance imaging of bone and muscle traits at the hip: an *in vivo* precision study. *J Musculoskelet Neuronal Interact* **14**, 104–110.
- Kuehn A, Simons ELR, Main RP (2017) The effect of growth rate and biomechanical loading on bone laminarity in the emu hindlimb. *FASEB J* **31**, 577.14.
- Kunz TH, Stern AA (1995) *Maternal investment and post-natal growth in bats*. Symposia of the Zoological Society of London.
- Lee AH, Simons ELR (2015) Wing bone laminarity is not an adaptation for torsional resistance in bats. *PeerJ* **2015**, e823.
- Lieberman DE, Polk JD, Demes B (2004) Predicting long bone loading from cross-sectional geometry. *Am J Phys Anthropol* **123**, 156–171.
- Maggiano C (2011) Making the mold: a microstructural perspective on bone modeling during growth and mechanical adaptation. In C. Crowder & S. Stout, eds. *Bone Histology: An Anthropological Perspective*. CRC Press, pp. 45–90.
- Maggiano I, Clement J, Thomas D, et al. (2015) Synchrotron three-dimensional reconstruction of cortical bone for analysis of osteonal branching and interconnectivity across age. *Am J Phys Anthropol* **156**, 210–211.
- Marelli CA, Simons ELR (2014) Microstructure and cross-sectional shape of limb bones in Great Horned Owls and Red-Tailed Hawks: how do these features relate to differences in flight and hunting behavior? *PLoS One* **9**, e106094.
- de Margerie E, Cubo J, Castanet J (2002) Bone typology and growth rate: testing and quantifying ‘Amprino’s rule’ in the mallard (*Anas platyrhynchos*). *C R Biol* **325**, 221–230.
- de Margerie E, Robin JP, Verrier D, et al. (2004) Assessing a relationship between bone microstructure and growth rate: a fluorescent labelling study in the king penguin chick (*Aptenodytes patagonicus*). *J Exp Biol* **207**(Pt 5), 869–879.
- de Margerie E, Sanchez S, Cubo J, et al. (2005) Torsional resistance as a principal component of the structural design of long bones: comparative multivariate evidence in birds. *Anat Rec A Discov Mol Cell Evol Biol* **282**, 49–66.
- Mitchell J, van Heteren AH (2015) A literature review of the spatial organization of lamellar bone. *CR Palevol* **15**, 23–31.
- Padian K, Werning S, Horner JR (2016) A hypothesis of differential secondary bone formation in dinosaurs. *CR Palevol* **15**, 41–49.
- Pearson OM, Lieberman DE (2004) The aging of Wolff’s ‘law’: ontogeny and responses to mechanical loading in cortical bone. *Am J Phys Anthropol* **125**(Suppl 39), 63–99.
- Pennycuik CJ (1967) The strength of the pigeon’s wing bones in relation to their function. *J Exp Biol* **46**, 219–233.
- Petrtyl M, Hert J, Fiala P (1996) Spatial organization of the haversian bone in man. *J Biomech* **29**, 161–169.
- Pratt IV, Cooper DML (2017) A method for measuring the three-dimensional orientation of cortical canals with implications for comparative analysis of bone microstructure in vertebrates. *Micron* **92**, 32–38.

- Pratt IV, Belev G, Zhu N, et al. (2015) *In vivo* imaging of rat cortical bone porosity by synchrotron phase contrast micro computed tomography. *Phys Med Biol* **60**, 211–232.
- Rensberger JM, Watabe M (2000) Fine structure of bone in dinosaurs, birds and mammals. *Nature* **406**, 619–622.
- deRicqlès AJ, Padian K, Horner JR, et al. (2000) Paleohistology of the bones of pterosaurs (Reptilia: Archosauria): anatomy, ontogeny, and biomechanical implications. *Zool J Linn Soc* **129**, 349–385.
- de Ricqlès A, Meunier F, Castanet J, et al. (1991) Comparative microstructure of bone. *Bone* **3**, 1–78.
- Rothschild BM, Panza RK (2007) Lack of bone stiffness/strength contribution to osteoarthritis – evidence for primary role of cartilage damage. *Rheumatology* **46**, 246–249.
- Seymour RS, Smith SL, White CR, et al. (2012) Blood flow to long bones indicates activity metabolism in mammals, reptiles and dinosaurs. *Proc R Soc B Biol Sci* **279**, 451–456.
- Sievänen H, Karstila T, Apuli P, et al. (2016) Magnetic resonance imaging of the femoral neck cortex. *Acta Radiol* **48**, 308–314.
- Skedros JG, Hunt KJ (2004) Does the degree of laminarity correlate with site-specific differences in collagen fibre orientation in primary bone? An evaluation in the turkey ulna diaphysis. *J Anat* **205**, 121–134.
- Starck JM, Chinsamy A (2002) Bone microstructure and developmental plasticity in birds and other dinosaurs. *J Morphol* **254**, 232–246.
- Swartz SM, Bennett MB, Carrier DR (1992) Wing bone stresses in free flying bats and the evolution of skeletal design for flight. *Nature* **359**, 726–729.
- Tafforeau P, Boistel R, Boller E, et al. (2006) Applications of X-ray synchrotron microtomography for non-destructive 3D studies of paleontological specimens. *Appl Phys A Mater Sci Process* **83**, 195–202.
- Turner CH, Burr DB (1993) Basic biomechanical measurements of bone: a tutorial. *Bone* **14**, 595–608.
- Wysokinski TW, Chapman D, Adams G, et al. (2007) Beamlines of the biomedical imaging and therapy facility at the Canadian light source – Part 1. *Nucl Instrum Methods Phys Res A* **582**, 73–76.
- Wysokinski TW, Chapman D, Adams G, et al. (2015) Beamlines of the biomedical imaging and therapy facility at the Canadian light source – part 3. *Nucl Instrum Methods Phys Res A* **775**, 1–4.
- Zebaze RM, Jones A, Welsh F, et al. (2005) Femoral neck shape and the spatial distribution of its mineral mass varies with its size: clinical and biomechanical implications. *Bone* **37**, 243–252.